

1 Constraints on early Mars atmospheric pressure 2 inferred from small ancient craters

3
4 Edwin S. Kite¹, Jean-Pierre Williams², Antoine Lucas¹, and Oded Aharonson^{1,3}

5
6 ¹ *Geological and Planetary Sciences, Caltech.*

7 ² *Earth and Space Sciences, University of California - Los Angeles.*

8 ³ *Helen Kimmel Center for Planetary Science, Weizmann Institute of Science, Israel.*

9
10 **The single most important control on long-term climate change on Mars is thought to be**
11 **decay of the CO₂-dominated atmosphere, but direct constraints on paleoatmospheric**
12 **pressure P are lacking¹. Of particular interest is the climate that allowed rivers to flow early**
13 **in Mars history, which was affected by P via direct and indirect greenhouse effects²⁻⁶. The**
14 **size of craters embedded within ancient layered sediments is a proxy for P : the smaller the**
15 **minimum-sized craters that form, the thinner the past atmosphere⁷⁻⁹. Here we use high-**
16 **resolution orthophotos and Digital Terrain Models (DTMs)¹⁰ to identify ancient craters**
17 **among the river deposits of Aeolis¹¹, and compare their sizes to models of atmospheric**
18 **filtering of impactors by thicker atmospheres¹²⁻¹³. The best fit is $P \leq 760 \pm 70$ mbar, rising to P**
19 **$\leq 1640 \pm 180$ mbar if rimmed circular mesas are excluded. Surveys tend to undercount**
20 **smaller craters, so these fits are upper limits. Our work assumes target properties**
21 **appropriate for desert alluvium¹⁴: if sediment developed bedrock-like rock-mass strength by**
22 **early diagenesis, the upper limit is greatly increased. If Mars did not have a stable multibar**
23 **atmosphere at the time that the rivers were flowing, the warm-wet CO₂ greenhouse of Ref. 2**
24 **is ruled out, and long-term average temperatures were probably below freezing⁴⁻⁶, implying**
25 **that exoplanet habitable-zone calculations that use Mars as a reference point may need to be**
26 **reconsidered¹⁵.**

27
28 Planetary atmospheres brake, ablate, and disrupt small asteroids and comets, filtering out small
29 hypervelocity surface impacts and causing fireballs, airbursts, meteors, and meteorites. The 2013
30 Chelyabinsk airburst destroyed an object that would have created a diameter (D) > 100 m crater in

31 the absence of an atmosphere. The smallest hypervelocity craters near sea-level on Earth have $D \sim$
32 20 m. “Zap pits” as small as 30 μm are known from the airless Moon, but other worlds show the
33 effects of progressively thicker atmospheres: the modern Mars atmosphere can remove >90% of
34 the kinetic energy of >240 kg impactors⁷; Titan’s paucity of small craters is consistent with
35 atmospheric filtering of craters smaller than 6-8km (Ref. 8); and on Venus, craters $D < 20$ km are
36 substantially depleted by atmospheric effects⁹.

37

38 Changes in the concentration of atmospheric volatiles are believed to be the single most important
39 control on Mars climate evolution and habitability, which in turn is a benchmark for habitable-
40 zone calculations for exoplanets¹⁵. Contrary to early work², it is doubtful that increasing CO_2
41 pressure (\approx total atmospheric pressure, P) is enough to raise early Mars mean-annual surface
42 temperature (\overline{T}) to the freezing point, even when water vapor and cloud feedbacks are
43 considered⁵. However, increased CO_2 aids transient surface liquid water production by impacts,
44 volcanism, or infrequent orbital conditions^{3-4,6}. Existing data requires an early epoch of massive
45 atmospheric loss to space; suggests that the present-day rate of escape to space is small; and offers
46 evidence for only limited carbonate formation¹⁶. These data have not led to convergence among
47 atmosphere evolution models, which must balance poorly understood fluxes from volcanic
48 degassing, escape to space, weathering, and photolysis¹⁷. More direct measurements¹⁸ are required
49 to determine the history of Mars’ atmosphere. Wind erosion exposes ancient cratered volumes on
50 Mars, and the size of exhumed craters has been previously suggested as a proxy of ancient Mars P
51 (e.g., Ref 19).

52

53 Here we obtain a new upper limit on early Mars atmospheric pressure from the size-frequency
54 distribution of small ancient craters interspersed with river deposits in Aeolis, validated using High
55 Resolution Imaging Science Experiment (HiRISE) DTMs and anaglyphs, in combination with
56 simulations of the effect of P on the crater flux. The craters are interbedded with river deposits up
57 to $\sim 10^3$ km long, with inferred peak river discharge 10-1000 m^3/s (Ref. 11). Therefore, the
58 atmospheric state they record corresponds to an era when Mars was substantially wetter than the
59 present, probably > 3.7 Ga (Supplementary Material).

60

61 **Data**

62 Aeolis Dorsa is a promising location to hunt for ancient craters: the stratigraphy is shot through
63 with the deposits of large rivers, and when these overlie a crater, that crater must be as ancient as
64 the rivers²⁰. Certain beds in Aeolis Dorsa (Supplementary Material) preserve a high density of
65 ancient craters, perhaps due to slow deposition or material properties unusually favorable for crater
66 preservation. We constructed stereo DTMs/orthophotos for two image-pairs covering these beds,
67 DTM1 and DTM2 (Methods). Following a checklist (Supplementary Table), craters were
68 classified as definite ancient craters (visibly embedded within stratigraphy: e.g., overlain by river
69 deposit) ($n = 56$, median diameter $D_{50} = 107$ m, 10th-percentile diameter $D_{10} = 50$ m), rimmed
70 circular mesas (RCM) ($n = 71$, $D_{50} = 48$ m, $D_{10} = 21$ m), or candidate ancient crater ($n = 192$, D_{50} also
71 48m, D_{10} also 21m; candidates are not considered further, but their inclusion would strengthen our
72 conclusions). We measured D by fitting circles to preserved edges/rims. RCM appear as disks in
73 raw HiRISE images. We interpret them as the erosionally-resistant fills/floors of impact craters
74 that were topographically inverted during the deflation of the target unit. They are unlikely to be
75 outliers of a young mantle because they are not found away from the fluvial unit. We plot them
76 separately, but consider them to be probable ancient craters. We used unambiguously ancient
77 craters as a guide to the preservation state of the smaller craters. These ancient craters are unlikely
78 to be maars; maars are not randomly distributed in space or time/stratigraphy. We also reject the
79 possibility that they are paleo-karst sinkholes; sinkholes lack rims, are concentrated at particular
80 stratigraphic levels, and are overdispersed.

81

82 **Model**

83 We generated synthetic crater populations for varying P (ref. 12). The approach is conceptually
84 similar to that of previous studies¹³, and benefits from measurements of the current Martian
85 cratering flux (Methods). We apply a geometric correction for exhumation from a cratered volume
86 (Supplementary Material) assuming that initial crater shape is isometric over the diameter range.
87 After bayesian fitting, we correct our P estimate for elevation (our DTMs are below datum; Mars-
88 average P was 20% lower than local P).

89

90 We do not track secondary craters, because meter-sized endoatmospheric secondaries are likely to
91 be braked to sub-hypervelocity speeds for the relatively thick atmospheres we are evaluating. In

92 other words, if wet-era small craters are secondaries, then early Mars' atmosphere was thin. A
93 caveat is that the impact blast will transiently modify local P .

94

95 **Paleopressure constraint**

96 We compared the model to the combined dataset (DTM1+DTM2). Combined best fits are $P =$
97 1640 ± 180 mbar, falling to $P = 760 \pm 70$ mbar if RCM (candidate syndepositional impact craters) are
98 also included (Figure 2). Because better preservation/exposure could allow still smaller embedded
99 craters to be uncovered, we interpret our fits as upper limits. The best fit to DTM1 (DTM2) ancient
100 craters alone is 1410 ± 250 mbar (1770 ± 250 mbar), falling to 830 ± 90 mbar (710 ± 80 mbar) if RCM
101 are included.

102

103 The results are sensitive to target strength, as expected²¹. Increasing the target rock-mass strength
104 to a hard-rock-like 6.9 MPa (ref. 22) increases the combined upper limit on P to ~ 1.8 bars. Our
105 work assumes weak soil-like target strength appropriate for river alluvium in an aggrading
106 sedimentary deposit: if sediment developed bedrock-like rock-mass strength by early diagenesis,
107 the upper limit is greatly increased. Sensitivity tests show a relatively minor effect of
108 fragmentation on the results (Supplementary Information).

109

110 We do not consider crater shrinkage or expansion by crater degradation. Only shrinkage matters
111 for the purpose of setting an upper bound on P : as the crater is abraded, the exposed radius must
112 eventually vanish. We surmise that shrinkage is a small effect because impact craters are bowl-
113 shaped (as opposed to cone-shaped), and because rims are frequently preserved.

114

115 **Environmental interpretation**

116 Our technique rules out a thick *stable* paleoatmosphere, and cannot exclude atmospheric collapse-
117 re-inflation cycles on timescales much shorter than the sedimentary basin-filling time. General
118 Circulation Model (GCMs) predict that atmospheric collapse to form CO₂-ice sheets and
119 subsequent re-inflation might be triggered by obliquity change (ref. 5). If sediment accumulated at
120 1-100 $\mu\text{m}/\text{yr}$ (ref. 20), our DTMs could integrate over $\sim 10^6$ - 10^8 years of sedimentation and contain
121 many collapse-and-reinflation cycles. Therefore one interpretation is that smaller ancient craters
122 formed while the atmosphere was collapsed, while rivers formed during high-obliquity, thick-

123 atmosphere intervals. However, published models indicate that collapse to form polar CO₂-ice
124 sheets only occurs for pressures less than our upper limit⁵.

125

126 Downward revisions to CO₂'s infrared opacity indicate that *any* amount of CO₂ is insufficient to
127 warm early Mars \overline{T} to the freezing point⁵. Even if further work incorporating radiatively-active
128 clouds moderates this conclusion, our result is an independent curb on stable CO₂/H₂O warm-wet
129 solutions (Figure 3). However, increased CO₂ below the warm-wet threshold primes Mars climate
130 for surface liquid water production by other relatively short-lived mechanisms, by adding to the
131 greenhouse effect, pressure-broadening the absorption lines of other gases⁴, suppressing evaporitic
132 cooling⁶, and increasing atmospheric heat capacity³.

133

134 If the small-crater limit is representative of early Mars P , no known mechanism allows continuous
135 stability of surface liquid water for the 10⁴-10⁵ yr needed to vertically integrate the hydrosphere.
136 This is true even with optimistic CO₂ radiative-forcing parameterizations. Transient warming by
137 eruptions, impacts, or infrequent orbital conditions could unfreeze the surface and shallow
138 subsurface, allowing runoff, but would not last long enough to unfreeze ground at ~1 km depth.
139 Therefore, atmospheric models do not support \overline{T} above freezing on early Mars, which has
140 implications for sedimentary-rock formation and diagenesis, groundwater hydrology, and
141 habitability.

142

143 **Synthesis of early Mars paleoatmospheric pressure**

144 Atmospheric loss must be part of the explanation for Mars' great drying, if only because
145 freshwater rivers cannot flow for hundreds of km when simultaneously boiling and freezing. How
146 high P was, and its decay over time, are not known. The 2014-2015 MAVEN mission will measure
147 modern loss processes.

148

149 Mars would have formed with ≥ 6 -10 bars CO₂-equivalent of carbon assuming the same initial [C]
150 and [Kr] as Earth. ⁴⁰Ar/³⁶Ar and ¹²⁹Xe/¹³²Xe suggest that 90-99% of the initial atmosphere was lost
151 prior to ~4.1 Ga. Subsequent loss rates are less clear; Mars' C/⁸⁴Kr ratio suggests $P \sim 60$ mbar
152 following the Late Heavy Bombardment¹.

153

154 Ref. 18 uses a volcanic bomb sag in Gusev Crater to infer $P > 120$ mbar from the bomb sag's
155 terminal velocity. This is consistent with our result. Our small-crater constraints on early Mars
156 atmospheric pressure are also congruent with isotopic and mineralogic indicators, which generally
157 require more assumptions than our method. For example, prehnite is observed on Mars²³ and is
158 unstable for CO₂ mixing ratios $>2 \times 10^{-3}$. This implies $P \lesssim 1$ bar, but only if water at depth was in
159 equilibrium with the atmosphere. The composition of a carbonate-rich outcrop at Gusev has been
160 interpreted to require $P = 0.5 - 2$ bars assuming that the carbonates are a solid solution in
161 thermodynamic equilibrium²⁴.

162

163 In the future, pyroclastic-blast runout length or even rainsplash²⁵ could be used to constrain P .
164 Curiosity's field site in Gale Crater contains syndepositional craters (Figure 1a), so Curiosity could
165 validate orbital identifications of embedded craters along its traverse. The 40-year-old prediction
166 of a connection between drying and atmospheric decay could be tested by applying the small-
167 crater technique to sedimentary deposits of different ages – ranging from Mawrth (the oldest
168 known sedimentary sequence in the Solar System), through Meridiani, to the relatively young
169 Valles Marineris silica deposits. This could yield a time series of constraints on early Mars
170 atmospheric pressure, stratigraphically coordinated to the sedimentary record of Mars' great
171 drying.

172

173 **Methods.**

174 **DTM generation.** DTMs were constructed following Ref. 10. MOLA Precision Experiment Data Records
175 (PEDRs) were used as ground control points. Optimal resolution depends on HiRISE image map scale
176 (0.25-0.5m), giving 1 – 2.5 m/post DTMs. Vertical precision is ~ 0.3 m, with 90% probability of precision
177 $\lesssim 1$ m (Supplementary Material).

178 **Cratering model.** We build a synthetic impactor population by drawing randomly from the size distribution
179 of Ref. 26 and the initial-velocity distribution of Ref. 27. Each population contains 3% irons, 29%
180 chondrites, 33% carbonaceous chondrites, 26% cometary objects, and 9% “soft cometary” objects
181 (following Ref. 28) with densities and ablation coefficients k_{ab} set following Ref. 28. We advect these
182 populations to the surface through atmospheres with scale height 10.7 km. The code does not track planet
183 curvature; we do not allow impactors to skip back to space. The atmosphere drains kinetic energy from
184 impactors via drag,

185

186

$$dv/dt = C_D \rho_a v^2 A \quad (1)$$

187

188 (we assume a drag coefficient $C_D = 1$ across the velocity (v) and size range of interest)

189

190 and ablation,

191

192

$$dm/dt = (C_h \rho_a v^3 A) / 2\zeta \quad (2)$$

193

194 where A is cross-sectional area, C_h is the heat transfer coefficient, and ζ is the heat of ablation.

195 Fragmentation occurs when ram pressure $\rho_a v^2$ exceeds M_{str} , disruption strength. M_{str} is set to 250 kPa; much

196 lower or much higher values would be inconsistent with the observation that $\frac{1}{2}$ of craters observed to form

197 in the current 6 mbar Mars atmosphere are clusters (Daubar et al., unpublished work). This value is within

198 the range reported for Earth fireballs²⁸; our conclusions are insensitive to M_{str} variations within Ref. 28's

199 range. Particles braked to <500 m/s would not form hypervelocity craters and are removed from the

200 simulation. Crater sizes are calculated using π -group scaling²², assuming target strength 65 kPa and target

201 density 2000 kg/m³ appropriate to cohesive desert alluvium¹⁴, and Holsapple scaling parameters $k_1=0.24$ and

202 $\mu=0.41$. Excavation efficiency decreases as $1/(v \sin \theta_i)$ where θ_i is the impact angle²⁹.

203

204 **References.**

205 1. Beaty, D.W., et al., Key science questions from the second conference on early Mars: Geologic,

206 hydrologic, and climatic evolution and the implications for life, *Astrobiology* **5**, 663-689 (2005).

207 2. Pollack, J.B., Kasting, J.F., Richardson, S.M., & Poliakov, K., The case for a wet, warm climate on early

208 Mars, *Icarus* **71**, 203-224 (1987).

209 3. Segura, T.L., Toon, O.B., Colaprete, A., Modeling the environmental effects of moderate-sized impacts

210 on Mars, *J. Geophys. Res.* **113**, E11007 (2008).

211 4. Tian, F., et al., Photochemical and climate consequences of sulfur outgassing on early Mars, *Earth &*

212 *Planet. Sci. Lett.* **295**, 412-418 (2010).

213 5. Forget, F., et al., 3D modelling of the early Martian climate under a denser CO₂ atmosphere:

214 Temperatures and CO₂ ice clouds, *Icarus* **222**, 81-99 (2013).

215 6. Kite, E.S., Halevy, I., Kahre, M.A., Wolff, M.J., Manga, M., Seasonal melting and the formation of

216 sedimentary rocks on Mars, with predictions for the Gale Crater mound, *Icarus* **223**, 181-210 (2013).

217 7. Chappelow, J.E., & Golombek, M.P., Event and conditions that produced the iron meteorite Block Island

218 on Mars, *J. Geophys. Res.* **115**, E00F07 (2010).

- 219 8. Wood, C.A., et al., Impact craters on Titan, *Icarus* **206**, 344-344 (2010).
- 220 9. Herrick, R.R., Sharpton, V.L., Malin, M.C., Lyons, S.N., and Feely, K. (1997), Morphology and
221 Morphometry of Impact Craters, pp. 1015-1046 in *Venus II*, eds. S. W. Bougher, D. M. Hunten, and R. J.
222 Phillips, U. of Arizona Press, Tucson, AZ (catalogue as v3; updated by R.R. Herrick in
223 <http://www.lpi.usra.edu/resources/vc/vchome.html>)
- 224 10. Kirk, R.L., et al., Ultrahigh resolution topographic mapping of Mars with MRO HiRISE stereo images:
225 Meter-scale slopes of candidate Phoenix landing sites, *J. Geophys. Res.* **113**, E00A24 (2008).
- 226 11. Burr, D.M., et al., Inverted fluvial features in the Aeolis/Zephyria Plana region, Mars: Formation
227 mechanism and initial paleodischarge estimates, *J. Geophys. Res.* **115**, E07011 (2010).
- 228 12. Williams, J.-P., Pathare, A., and Aharonson, O., Modeling small impact populations on Mars, EPSC
229 abstracts, vol 7, EPSC2012-95 (2012).
- 230 13. Popova, O., Nemtchinov, I., & Hartmann, W.K., Bolides in the present and past martian atmosphere and
231 effects on cratering processes, *Meteor. & Planet. Sci.* **36**, 905-925 (2003).
- 232 14. Holsapple, K.A., and Housen K.R., A crater and its ejecta: An interpretation of Deep Impact, *Icarus*
233 **191**(2:Supplement), 586-597 (2007).
- 234 15. Kopparapu, R.K., et al., Habitable zones around main-sequence stars: New estimates, *Astrophys. J.*
235 **765**:131 (2013).
- 236 16. Lammer, H., et al. Outgassing history and escape of the Martian atmosphere and water inventory,
237 *Space. Sci. Rev.* **174**, 113-154 (2013).
- 238 17. Manning, C.V., McKay, C.P., and Zahnle, K.J., Thick and thin models of the evolution of carbon
239 dioxide on Mars, *Icarus* **180**, 38-59 (2006).
- 240 18. Manga, M., A. Patel, J. Dufek and E.S. Kite, Wet surface and dense atmosphere on early Mars inferred
241 from the bomb sag at Home Plate, Mars, *Geophys. Res. Lett.* **39**, L01202, doi:10.1029/2011GL050192
242 (2012).
- 243 19. Vasavada, A.R., Milavec, T.J., and Paige, D.A., Microcraters on Mars: Evidence for Past Climate
244 Variations, *J. Geophys. Res.* **98**, 3469-3476 (1993).
- 245 20. Kite, E.S., Lucas, A.S., and Fassett, C.I., Pacing Early Mars river activity: Embedded craters in the
246 Aeolis Dorsa region imply river activity spanned $\geq(1-20)$ Myr, *Icarus* in press,
247 doi:10.1016/j.icarus.2013.03.029 (2013).
- 248 21. Dundas, C.M., Keszthelyi, L.P., Bray, V.J., and McEwen A.S., Role of material properties in the
249 cratering record of young platy-ridged lava on Mars, *Geophys. Res. Lett.* **37**, L12203 (2010).
- 250 22. Holsapple, K.A., The scaling of impact processes in planetary sciences, *Ann. Rev. Earth Planet. Sci.* **21**,
251 333-373 (1993).

- 252 23. Ehlmann, B.L., et al., Evidence for low-grade metamorphism, hydrothermal alteration, and diagenesis
253 on Mars from phyllosilicate mineral assemblages, *Clays and Clay Minerals* **59**, 359-377 (2011).
- 254 24. van Berk, W., Fu, Y., Ilger, J.-M., Reproducing early Martian atmospheric carbon dioxide partial
255 pressure by modeling the formation of Mg-Fe-Ca carbonate identified in the Comanche rock outcrops on
256 Mars, *J. Geophys. Res.* **117**, E10008 (2012).
- 257 25. Som S., Catling D., Harnmeijer J., Polivka P., & Buick R., Air density 2.7 billion years ago limited to
258 less than twice present levels by fossil raindrop imprints. *Nature* **484**, 359 – 362 (2012).
- 259 26. Brown P., Spalding, R. E., ReVelle, D.O., Tagliaferri, E. & S. P. Worden, The flux of small near-Earth
260 objects colliding with the Earth. *Nature* **420**, 294–296 (2002).
- 261 27. Davis, P., Meteoroid impacts as seismic sources on Mars, *Icarus* **105**, 469-478 (1993).
- 262 28. Ceplecha, Z., et al., Meteor phenomena and bodies, *Space Sci. Rev.* **84**, 327-341 (1998).
- 263 29. Pierazzo, E., & H.J. Melosh, Understanding oblique impacts from experiments, observations, and
264 modeling, *Annu. Rev. Earth Planet. Sci.* **28**, 141-168 (2000).
- 265 30. Cassata, W. et al., Trapped Ar isotopes in meteorite ALH 84001 indicate Mars did not have a thick
266 ancient atmosphere, *Earth Planet. Sci. Lett.* **221**, 461-465 (2012).

267

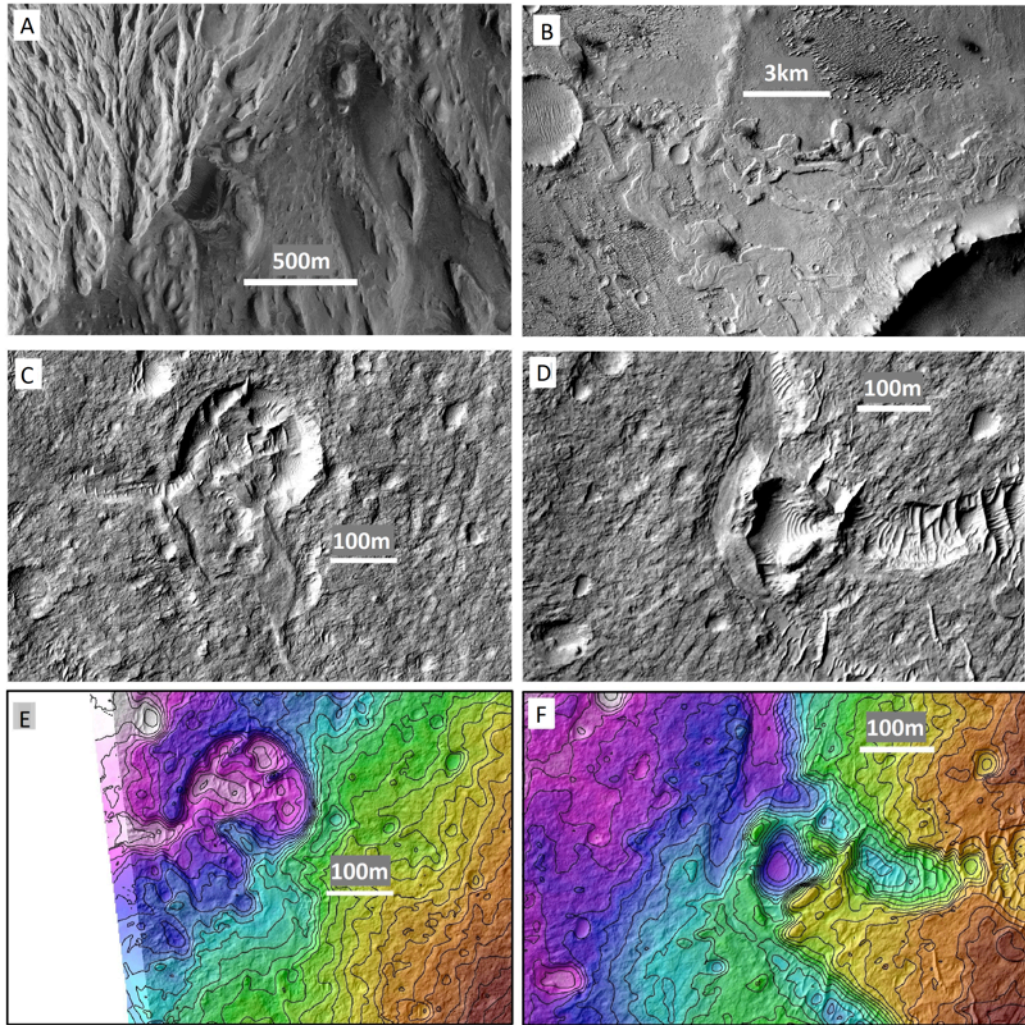
268 **Author contributions**

269 E.S.K. designed research, picked craters, carried out the data-model comparison, and drafted the main text.
270 J.-P.W. wrote the forward model of impactor-atmosphere interactions. A.L. built the digital terrain models
271 and wrote the corresponding Supplementary text. O.A. supervised research. All authors contributed to the
272 interpretation of the results and to the revisions.

273 **Acknowledgements.** We thank Ingrid Daubar, Joe Dufek, Bethany Ehlmann, Woody Fischer, Vamsi Ganti,
274 Itay Halevy, Kevin Lewis, Michael Manga, Ramses Ramirez, Melissa Rice, and Alejandro Soto for
275 preprints and discussions. This work was funded by an O.K. Earl Fellowship (to E.S.K.) and NASA grants
276 NNX11AF51G (to O.A.) and NNX11AQ64G (to J.-P.W.)

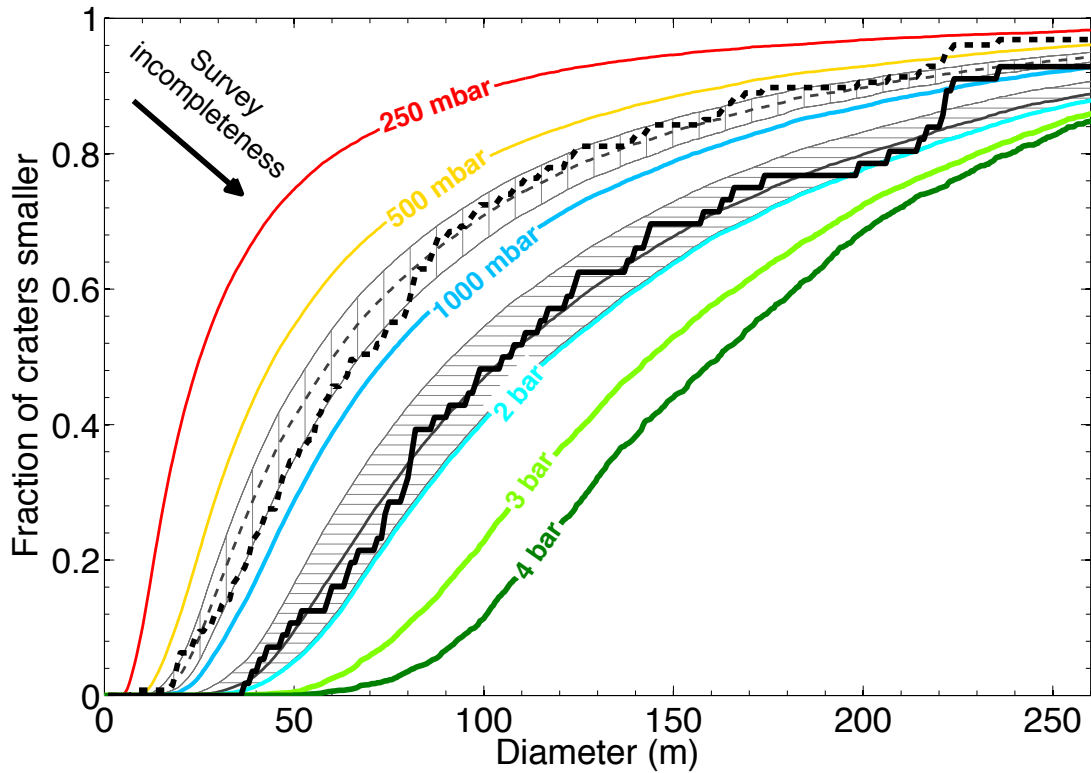
277

278 **Figures.**



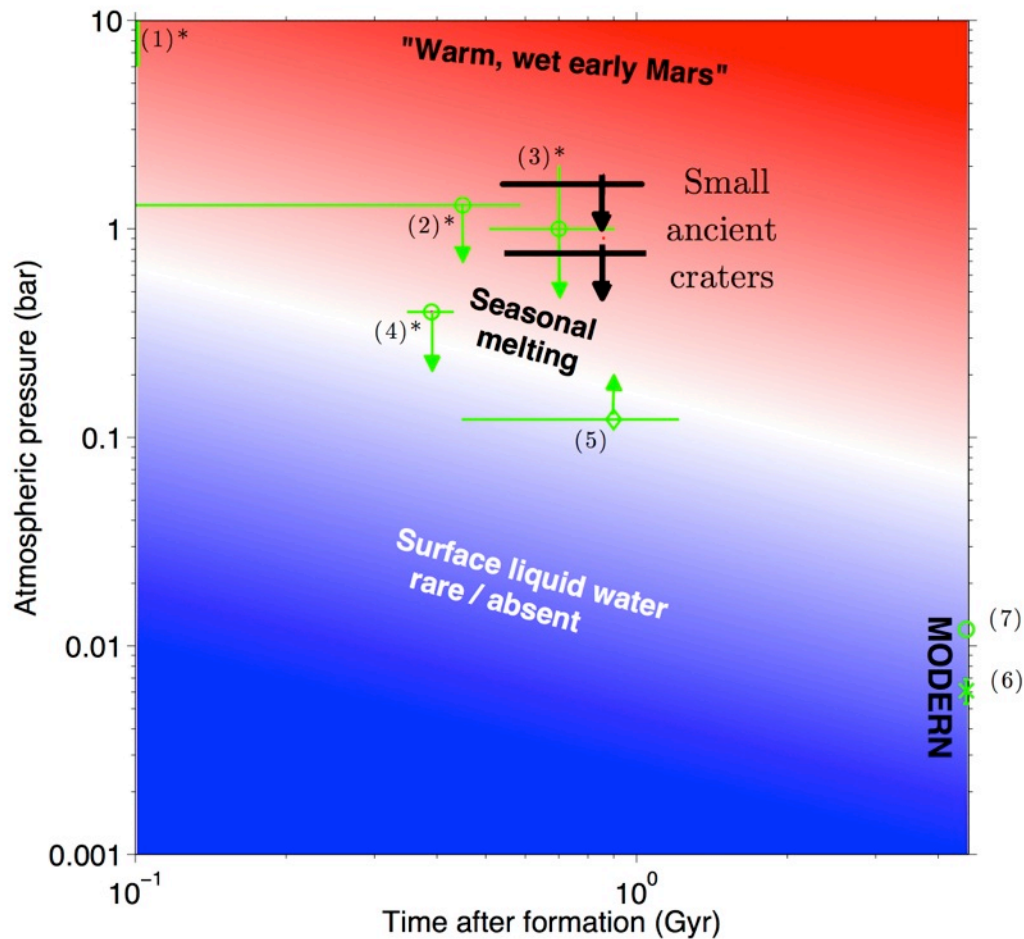
279

280 **Figure 1. Gallery of ancient Martian craters** (after Ref. 20). a) Crater being exhumed from
281 beneath an unconformity within Gale Crater's mound (Aeolis Mons/Mt. Sharp), the destination of
282 the Curiosity rover. ESP_019988_1750. b) Craters with fresh-appearing ejecta being exhumed
283 from beneath meander belts, Aeolis Dorsa, P15_006973_1742_XI_05S205W; Ref. 11. c) Crater
284 being exhumed from beneath fluvial channel deposit, Aeolis Dorsa. 238 m diameter.
285 ESP_019104_1740. d) Crater draped by fluvial channel deposit, Aeolis Dorsa, ESP_019104_1740.
286 141m diameter. e) Crater from (c), but with 1m elevation contours from DTM2 (see text). f) Crater
287 from (d), with 1m contours from DTM2.



288

289 **Figure 2. Upper limits on Early Mars atmospheric pressure:** comparison of model crater size-
 290 frequency distributions to observations. Solid black line corresponds to definite embedded craters.
 291 Dashed black line additionally includes rimmed circular mesas. Stair-stepping in the data curves
 292 corresponds to individual craters. Colored lines show model predictions for atmospheric filtering
 293 of small impactors at different pressures. Gray hatched regions correspond to 2σ statistical-error
 294 envelope around the best-fit paleopressure to the data (best fit shown by thick gray lines). Survey
 295 incompleteness leads to overestimates of median crater size, so best fits are upper limits.



297

298 **Figure 3. Paleopressure constraints on the great drying of Mars.** Black symbols show the
 299 upper limit from small-ancient-craters described here, and green symbols are other estimates
 300 discussed in the text (asterisks mark indirect estimates):- (1*) initial cosmochemical estimate¹;
 301 prehnite²³ stability; (3*) carbonate Mg/Ca/Fe (ref. 24); (4*) ⁴⁰Ar/ ³⁶Ar (ref. 30); (5) bomb sag¹⁸;
 302 modern seasonal range; (7) modern seasonal range + observed buried South Polar CO₂ ice.
 303 Implications for sustained surface habitability are shown by background colors, from blue for too
 304 cold for melting to red for melting year-round. These are approximate and model-dependent, for
 305 example the snowmelt threshold is sensitive to assumed snowpack thermal inertia⁶. Melting is
 306 much more difficult under the faint young Sun. “Warm, wet early Mars” refers to the long-term
 307 stable climate solution of Ref. 2. Age estimates are detailed in Supplementary Material.
 308

309 **Supplementary Material.**

310

311 **Contents: Supplementary Text, Supplementary Table 1, Supplementary Figures 1-8.**

312

313 **1. Geologic Constraints and Geologic Context**

314

315 **1a. Stratigraphic Control**

316 Stratigraphic relations prove that our DTMs sample near the center of a thick interval of fluvial
317 deposition, and do not represent the final gasp of large-river activity. The most recent published
318 map covering Aeolis Dorsa is Zimbelman & Scheidt (2012). Our DTMs straddle the contact of two
319 fluvial units within the area mapped by Zimbelman & Scheidt as “AHm11” (Fig. S1). These units
320 are traceable for >300 km. The lower of the two units, which we informally term F1 (Fluvial 1), is
321 defined by broad meander-belts, often with multiple preserved generations of cutoff and/or cut-
322 and-fill. Material laterally adjacent to channel belts erodes to form yardangs, leaving the meander-
323 belts as locally high-standing features. F1 is overlain, apparently conformably, by F2 (Fluvial 2).
324 Our DTMs overlie this contact. F2 is a slope-forming unit, densely peppered with rimless craters,
325 interpreted as impact craters. Across Aeolis Dorsa, F2’s crater density is higher than that of the
326 units which envelop it, especially near the contact with F1. F2 is associated with young aeolian
327 bedforms, and we interpret the sediment source for these bedforms to be erosion of F2. The
328 erosional expression of channels in F2 is variable, but relative to channels in F1 they are typically
329 narrower, have more frequent confluences, form more tree-like as opposed to subparallel networks,
330 and are more frequently preserved in negative relief than are channels in F1. F2 is >100m thick
331 and is overlain by additional channel-containing units (not obviously exposed in our DTMs) that
332 feature channel belts wider than those in F2. In all cases, channels show little relationship to the
333 modern topography and are eroding out of the rock: F2 channels postdate F1 channels. The base of
334 F1 is not exposed near our study region but it is at least tens of meters below the F1-F2 contact.
335 Because our DTMs sample at/near the base of thick channel-containing unit that is overlain by
336 further channel-containing units, we conclude that our *P* constraint corresponds to the heart of a
337 major river-forming time interval on Mars (conceivably, the *only* major river-forming time interval
338 on Mars; Howard et al., 2005). The total stratigraphic interval over which fluvial deposits are
339 abundant in Aeolis Dorsa is >300m.

340

341 The simplest interpretation of the interfluvial terrain in both F1 and F2 is as the overbank deposits of
342 rivers, but other interpretations are possible. For example, the river deposits could be the fill of
343 incised valleys that postdate the interfluvial materials.

344

345 **1b. Age Control**

346 The craters date from around the time when large rivers flowed on the surface of Mars; they are
347 almost certainly pre-Amazonian, and probably Early Hesperian or older. We carried out a CTX
348 crater count over an $8 \times 10^4 \text{ km}^2$ region largely conterminous with Aeolis Dorsa, dividing craters $>$
349 1 km into postfluvial, synfluvial/prefluvial, and undetermined on the basis of local crosscutting
350 relationships. Using the standard definition (Werner & Tanaka, 2011) of $N(x)$ as the frequency of
351 craters with $D > x \text{ km}$ per 10^6 km^2 count area, $N(1)$ is 1049 ± 113 for postfluvial craters and
352 2049 ± 158 for postfluvial+undetermined craters. $N(2)$ is 415 ± 71 for postfluvial craters and 634 ± 88
353 for postfluvial+undetermined craters. $N(5)$ is 37 ± 21 for postfluvial craters, and there are no
354 undetermined craters in this size class. Based on crater morphology we think most of the
355 ‘undetermined’ craters are in fact postfluvial, implying a $N(1)$ Crater-Retention Age (CRA) on the
356 Hesperian/Amazonian boundary and an $N(2)$ CRA straddling the Late Hesperian/Early Hesperian
357 boundary (Werner & Tanaka, 2011). Stratigraphic relations (Zimbelman & Scheidt, 2012), and
358 evidence in the form of mesas for removal of several hundreds of meters of overburden, further
359 support our inference that the rivers flowed in the Hesperian or Noachian. This is because removal
360 would lead to loss of craters, so our CRAs are minima. Our DTMs lie within a region of Aeolis
361 Dorsa that has an unusually low $N(1)$: if this results from relatively rapid exhumation, consistent
362 with the excellent preservation state of the ancient rivers, a resurfacing rate of $\sim 1 \mu\text{m/yr}$ is implied
363 over 10^{8-9} yr timescales. Relatively rapid modern erosion, combined with a high embedded-crater
364 density, makes this a particularly attractive site for our procedure: rapid erosion minimizes the
365 proportion of geologically-recent (synerosional) craters in the distribution, and thus the impact of
366 false positives (assuming the false positive error rate is fixed). Our results are consistent with
367 Zimbelman & Scheidt (2012), who additionally suggest that the rivers (i.e. Zimbelman & Scheidt’s
368 “AHm1”) predate a topographically highstanding unit (their “Hm”) with a $\sim 3.7 \text{ Ga}$ CRA on the
369 Hartmann & Neukum (2001) chronology. Regional geology as mapped by Irwin et al. (2010)
370 implies that the rivers are not older than Late Noachian.

371 For the other data points in Figure 3:- the prehnite (“2*”) age estimate assumes prehnite formation
372 prior to the Isidis impact (Fassett & Head, 2011), consistent with although not required by geologic
373 relations (Ref. 23); the carbonate Mg/Ca/Fe (“3*”) age estimate assumes that the Comanche
374 outcrop formed after the Gusev impact but prior to the Gusev plains lavas (Greeley et al., 2005);
375 for the $^{40}\text{Ar}/^{36}\text{Ar}$ age constraint (“4*”) we use the 4.16 ± 0.04 Ga age adopted by Ref. 30; and for the
376 bomb sag (“5*”) age estimate we assume a pre-Amazonian age. All of these ages – with the
377 possible exception of the ALH 84001 age – may need later revision; the crater chronology of early
378 Mars has not yet been securely calibrated to radiogenic dates (Robbins et al., 2013).

379

380 **2. Details of Small Crater Analysis**

381 Our model uses a modern (Near Earth Object-like) size-frequency distribution of impactors, which
382 is relatively rich in small impactors due to the Yarkovsky effect (Strom et al., 2005). This is
383 appropriate for stratigraphic units postdating the Late Heavy Bombardment (see discussion of
384 “Age Control” above); the large rivers on Mars that have been mapped so far were last active
385 significantly after the Late Heavy Bombardment (Fassett & Head, 2008; Hoke & Hynes 2009). If
386 we are wrong and the rivers date from the time of the Late Heavy Bombardment, then the small-
387 impactor-poor impactor size-frequency distribution inferred for the Late Heavy Bombardment by
388 Strom et al. (2005) may be appropriate. In that case, the observation of a large proportion of small
389 impact craters requires an even lower P than reported here, and our paleopressure conclusions are
390 strengthened.

391

392 When craters are dispersed through a 3D volume, the size-frequency distribution of exhumed
393 craters will favor larger craters because a 2D surface cutting through the volume (i.e., the erosion
394 surface) is more likely to intersect a big crater than a small one. This geometric exposure
395 correction is proportional to crater size if craters of different sizes have the same shape, which is
396 approximately true in the strength regime relevant to this paper (Melosh, 1989). Therefore, we
397 apply a correction proportional to crater size.

398

399 Small craters can be thought of as tracer particles with respect to erosion and sedimentation
400 processes. Scale-independence of erosion and sedimentation events (the Sadler effect; Jerolmack
401 & Sadler, 2007; Schumer & Jerolmack, 2009) will tend to preferentially obliterate smaller craters

402 (Ref. 20). This is because smaller craters are more likely to be completely removed with the
403 ‘Cantor dust’ of scale-independent erosion events. This effect is independent of the purely
404 geometric exposure effect discussed above, although it has the same sign. If the Sadler effect were
405 important for ancient sedimentation on Mars, this would bias our survey towards detecting larger
406 craters. We do not attempt to correct for this bias because we do not know if the Sadler effect was
407 important for ancient sedimentation on Mars. Any correction would lower our paleopressure upper
408 bound, strengthening our conclusions.

409

410 Erosion may modify craters. The main defense against this is to fit the circles defining the crater
411 diameters only to parts of the crater edge which are well-preserved. A supplementary defense is to
412 expand (or contract) the resulting circles until they enclose only two (or enclose all *except* two) of
413 the hand-picked points on the crater rim. We then define the annulus enclosed by these minimal
414 and maximal craters as a ‘preservation-error annulus.’ We found no significant difference between
415 total errors (from resampling) including random sampling of radii from within the preservation-
416 error annulus as opposed to total resampling errors excluding this effect. Therefore, we do not
417 include this additional error in our final paleopressure estimate.

418

419 We do find one cluster of large ancient craters (in the SE of DTM 1), which may result from
420 dispersal of secondaries in a thicker atmosphere (Popova et al., 2007). It is possible that future
421 work might use ancient crater clusters to set a lower limit on atmospheric paleopressure.

422

423 We do not use the ‘candidate’ exhumed craters – which by definition are not definitely exhumed -
424 because they may be significantly contaminated by synerosional craters. The regional $N(1)$ count is
425 consistent with a landscape that is currently being sanded down at $1 \mu\text{m}/\text{yr}$, which (assuming
426 steady state resurfacing with equilibrium between production and obliteration, and ignoring
427 aeolian bedforms) could permit a considerable number of degraded synerosional craters to form in
428 the modern thin atmosphere. However, we do not see many pristine (rayed, blocky, or deep) $D \sim$
429 50m craters. It is possible that the balance is made up by ‘candidate’ exhumed craters that are in
430 fact relatively recent synerosional craters which have lost their rims. This is supported qualitatively
431 by evidence of rapid small-crater degradation along the Opportunity traverse (Golombek et al.,
432 2010). Some evidence for this suspicion comes from the cumulative size-frequency distribution of

433 candidate craters. On a log-log plot of cumulative crater-size frequency distributions (e.g., Werner
434 & Tanaka, 2011), the zero-atmosphere power-law slope (dN_{cum}/dD) on a pristine, stable surface is
435 close to -3 for the 20-500m diameter craters of interest. This exponent is shallowed by the
436 geometric correction for dispersal through a 3D volume ($\Delta = +1$), by atmospheric filtering ($\Delta = +0$
437 to +0.5, increasing with pressure), and by preferential preservation/detection of large craters. The
438 size-frequency distribution of the ‘candidate’ craters is not as shallow as would be expected if all
439 of these craters were exhumed. If we are wrong and the candidate exhumed craters are all
440 syndepositional, our paleopressure upper bound would be lowered by a factor of ~ 2 , strengthening
441 our conclusions.

442

443 We interpret craters mapped as ‘ancient’ that lie between the river deposits as being part of the
444 same (buried/embedded) crater population as craters that are overlain by ancient river deposits. If
445 this interpretation is correct, a histogram of river-crater interaction frequencies from a Monte Carlo
446 trial should be consistent with the mapped population. But if our false positive rate is significantly
447 higher away from the river deposits, this would show up as a reduced proportion of river-crater
448 interactions relative to that expected by chance. For long, parallel river deposits of spacing W and
449 crater diameter $<$ river-deposit width, the fraction of intersections is approximately D/W . This is
450 consistent with our mapped populations if we make the approximation $W = A/L$ where A is DTM
451 area and L is channel length. However, the geometry of the real river deposits is more complicated
452 than this idealization (Fig. S8). Therefore, to validate our interpretation, we did the following
453 (typical output shown in Fig. S2):-

454

- 455 (1) Mapped the outlines of all channels within the DTMs (Fig. S8);
- 456 (2) Sprinkled random crater populations over the resulting maps, randomizing locations and
457 randomly selecting radii from the observed populations. The number of ‘definite’ craters
458 and the number of rimmed circular mesas is the same as in the mapped distribution. Craters
459 100% obscured by channel deposits were removed with replacement;
- 460 (3) Counted the number of crater-river interactions for this synthetic population (and the areas
461 of overlap);
- 462 (4) Repeated 1,000 times.

463

464 We found that the ‘preferred’ crater population is in the 56th percentile of the synthetic distribution
465 of crater-river interaction frequencies (Fig. S2). The ‘definite’ crater population has *more* river-
466 crater interactions than 89% of the synthetic populations, which may indicate a higher likelihood
467 that true embedded craters are relegated to ‘candidate’ status away from the river deposits. The
468 Rimmed Circular Mesas have a lower interaction frequency than 90% of the random populations,
469 probably because they are locally high-standing so that horizontally-adjacent river deposits have
470 usually been eroded away. This procedure obviously cannot rule out a small contribution of false
471 positives, but in combination with our geologic checklist (Supplementary Table 1) it validates our
472 interpretation that ancient craters mapped as ‘definite’ between the river deposits do not have a
473 significantly higher false positive rate than ancient craters mapped as ‘definite’ that underly river
474 deposits.

475

476 **3. Details of data-model comparison and sensitivity tests**

477 More details about our forward model of impactor-atmosphere interactions can be found in
478 Williams et al. (2010) and Williams & Pathare (2012). The small-craters technique has been
479 previously applied by Kreslavsky (2011) and Paige et al. (2007) to infer P for relatively recent
480 Martian deposits. We adopt an impactor entry angle distribution that peaks at 45° (Love and
481 Brownlee, 1991). Modeled smallest-crater size increases linearly from ~ 20 m at 1 bar to ~ 100 m at
482 5 bars, as expected from equating impactor and atmospheric-column masses (Melosh, 1989). This
483 is broadly consistent with low-elevation impacts on Earth (the column mass of Earth’s sea-level
484 atmosphere is equivalent to ~ 400 mbar on Mars). Therefore, we linearly interpolate model output
485 between runs at 0.125, 0.25, 0.5, 1.0, 2.0, 3.0, and 5.0 bars to obtain crater size-frequency
486 distributions as a function of P .

487

488 Atmospheric pressure was found by fitting the data to cratering-model output, treating the impacts
489 as a Poisson process (e.g. Wall & Jenkins, 2012; Aharonson et al., 2003). The prior is flat in log
490 paleopressure. The impact size-frequency distribution is modeled as a function of atmospheric
491 pressure and a flux scaling parameter only. At first, we marginalized over the flux scaling
492 parameter, but in practice we found that we obtained almost the same results by using a single flux
493 scaling parameter chosen to produce the same number of craters as observed. When fitting the data
494 to the model, the crater diameters are binned in increments of 1m. Diameters < 10 m are excluded

495 from the fit. This excludes one RCM. Including this RCM lowers paleopressures by ~ 100 mbar,
496 because such a small crater is a very improbable (although singular) event under a thick
497 atmosphere. Our procedure is analogous to χ -squared fitting, but it is appropriate for the limit
498 where each bin contains a small number of data.

499

500 The most important parameter sensitivity of the model is to target strength. The strongest rock
501 targets produce a factor-of-2 decrease in crater size (Refs. 21, 22), and a comparable increase in
502 the paleopressure upper bound (Fig. S3b) relative to our preferred rock-mass strength of 65 kPa.
503 Our main argument against adopting strong-rock rock-mass-strength for our model is geological –
504 because of the observed high density of river deposits in the terrain (Refs. 11, 20; Fig. S1), the
505 simplest interpretation of geological units “F1” and “F2” is that they are fluvial/alluvial or other
506 weak sedimentary deposits, analogous to terrestrial desert alluvium. Desert alluvium has been
507 thoroughly characterized through Nevada Test Site explosions of comparable energy to the small
508 natural hypervelocity impact craters used in this paper, and an empirical rock-mass strength of ~ 65
509 kPa is inferred. This is the value that we use in this paper. Crucially, the *present-day* outcrop
510 strength of the Aeolis Dorsa deposits is irrelevant, because embedded craters formed early in the
511 history of the deposits and the timing of any compaction or cementation is unknown. Model output
512 is not very sensitive to the details of how fragmentation is parameterized (Fig. S3a), to target
513 density (Fig. S3c), or to reasonable variations in the mix of impactor strengths and densities (e.g.,
514 the stone:iron ratio; not shown).

515

516 We limit the computational cost of the model by only injecting impactors at the top-of-the-
517 atmosphere that are larger than a cutoff diameter d_c . Holding d_c constant over the wide range of
518 pressures of interest leads to interminably long runs for high atmospheric pressures. This is
519 because building up a smooth cdf of predicted crater diameters requires hundreds of large
520 impactors, but most CPU time is wasted on detailing the fate of numerous small impactors which
521 have a vanishingly small chance of forming hypervelocity craters. Therefore, we chose increasing
522 cutoff diameters for increasing atmospheric pressure. These $d_c(P)$ were set for each P by
523 progressively decreasing the cutoff diameter from a large value until further reductions did not
524 lead to a significant change in model output crater cdf.

525

526 **4. DTM extraction procedure**

527 The procedure used for DTM extraction follows that of Ref. 10 and uses the NGATE algorithm
528 (Zhang, 2006) and SOCET SET software. The HiRISE images making up the
529 PSP_007474_1745/ESP_024497_1745 stereopair have emission angle of 4.5 degrees and 30
530 degrees respectively, and a map scale of 25cm/pixel and 50cm/pixel respectively. The coarser
531 image (ESP_024497_1745 in this case) controls the optimal spatial resolution for the topographic
532 extraction, so we derived a 2.5 m/post DTM for this pair (DTM1). MOLA PEDRs were used as
533 ground control points, with vertical accuracy set to 10 m, as the area contains mostly flat smooth
534 features, for which it is difficult to link PEDR shots to surface features observed as HiRISE scale.
535 In addition, we generated our own gridded MOLA DTM (from PEDR), which we used as a seed
536 for extraction. The process for DTM2 was very similar (emission angles 2 and 18 degrees; map
537 scales of 50cm/pixel for both images).

538

539 We used several metrics for DTM validation and quality assessment. These included LE90 (Linear
540 Error of 90%). This value is automatically computed (by the SOCET SET photogrammetry
541 software) as the error in elevation of one point with respect to another point within the DTM at
542 90% probability. In DTM1, the mean LE90 is 1.07 m and when correlation had succeeded, the
543 highest value is 3 m. These values should be compared with the theoretical limit
544 on vertical precision using the standard photogrammetry equation (Ref. 10):

545

546

$$EP = r s / (b/h)$$

547

548 where EP is the expected vertical precision, r is the accuracy with which features can be matched
549 (i.e., $r=0.3$), s the ground sample distance (i.e., $s = 50$ cm), and the b/h ratio describes the
550 convergence geometry of the stereo pair (i.e., $b/h \sim 0.5$). These values give $EP \sim 0.3$ m. As a test,
551 the shaded relief was compared to the orthophoto using the same illumination geometry over a
552 constant albedo area (Fig. S4, S5). Figure S6 presents cross-sections over both the HiRISE image
553 and the shaded relief computed from the DTM. A good match is obtained.

554

555

556

557 **Supplementary References.**

- 558 Aharonson, O., Schorghofer, N., & Gerstell, M.F., Slope streak formation and dust deposition rates on
559 Mars, *J. Geophys. Res.* **108**, 5138, (2003).
- 560 Fassett, C.I., & Head, J.W. The timing of martian valley network activity: Constraints from buffered crater
561 counting. *Icarus* **195**, 61–89 (2008).
- 562 Fassett, C.I., & Head, J.W. Sequence and timing of conditions on early Mars. *Icarus* **211**, 1204-1214
563 (2011).
- 564 Golombek, M., et al., Constraints on ripple migration at Meridiani Planum from Opportunity and HiRISE
565 observations of fresh craters: *J. Geophys. Res.* **115**, E00F08, doi:10.1029/2010JE003628 (2010).
- 566 Greeley, R., et al., Fluid lava flows in Gusev crater, Mars, *J. Geophys. Res.*, **110**, E05008,
567 doi:10.1029/2005JE002401 (2005).
- 568 Hartmann, W.K. & Neukum, G., Cratering Chronology and the Evolution of Mars,
569 *Space Sci. Rev.* **96**, 165-194 (2001).
- 570 Hoke, M.R.T., & Hynek, B.M., Roaming zones of precipitation on ancient Mars as recorded in valley
571 networks, *J. Geophys. Res.* **114**, E08002 (2009).
- 572 Howard, A.D., Moore, J.M., & Irwin, R.P., An intense terminal epoch of widespread fluvial activity on
573 early Mars: 1. Valley network incision and associated deposits, *J. Geophys. Res.* **110**, E12S14 (2005).
- 574 Irwin, R.P., & Watters, T.R., Geology of the Martian crustal dichotomy boundary: Age, modifications, and
575 implications for modeling efforts, *J. Geophys. Res.* **115**, E11006 (2010).
- 576 Jerolmack, D.J. & Sadler, P., Transience and persistence in the depositional record of continental margins.
577 *J. Geophys. Res.*, **112**, F03S13 (2007).
- 578 Kreslavsky, M. A., Observational constraints on atmospheric pressure on Mars in the Amazonian, *Fourth*
579 *International Workshop on the Mars Atmosphere: Modelling and observation*, Paris, France (2011).
- 580 Love, S.G. & Brownlee D.E., Heating and thermal transformation of micrometeoroids entering the Earth's
581 atmosphere, *Icarus* **89**, 26-43 (1991).
- 582 Melosh, H.J. *Impact cratering: A geologic process*, Oxford University Press, Oxford, UK (1989).
- 583 Paige, D.A., et al., (2007), MER small crater statistics: Evidence against recent quasi-periodic climate
584 variations, in *7th Intl. Conf. on Mars*, 3392 (2007).
- 585 Popova, O.P., et al., Crater clusters on Mars: Shedding light on martian ejecta launch conditions, *Icarus*
586 **190**, 50-73 (2007).
- 587 Robbins, S.J., Hynek, B.M., Lillis, R.J., & Bottke, W.F., Large impact crater histories of Mars: the effect of
588 different model crater age techniques, *Icarus*, doi: 10.1016/j.icarus.2013.03.019 (2013).
- 589 Schumer, R., & Jerolmack, J.D., Real and apparent changes in sediment deposition rates through time, *J.*
590 *Geophys. Res.* **114**, F00A06 (2009).

591 Strom, R.G., et al., The Origin of Planetary Impactors in the Inner Solar System, *Science* **309**, 1847 (2005).
592 Wall, J.V. & Jenkins, C.R., Practical statistics for astronomers, 2nd Edition (Cambridge Observing
593 Handbooks for Research Astronomers), Cambridge University Press, Cambridge, UK (2012).
594 Werner, S.C. & Tanaka, K.L., Redefinition of the crater-density and absolute-age boundaries for the
595 chronostratigraphic system of Mars. *Icarus* **215**, 603-607 (2011).
596 Williams, J.-P., Aharonson, O., & Pathare, A.V., The production of small primary craters on Mars, in 41st
597 *Lunar Planet. Sci. Conf.*, 2574 (2010).
598 Williams, J.-P., & Pathare, A.V., Scaling effective diameters of small impact crater clusters on Mars, in 43rd
599 *Lunar Planet. Sci. Conf.*, #2881 (2012).
600 Zhang, B., Towards a higher level of automation in softcopy photogrammetry: NGATE and LIDAR
601 processing in SOCET SET®, paper presented at GeoCue Corporation 2nd Annual Technical Exchange
602 Conference, Nashville, Tenn. (2006).
603 Zimbelman, J.R., & Scheidt, S.P., Hesperian age for Western Medusae Fossae Formation, Mars. *Science*
604 **336**, 1683 (2012).

605 **Supplementary Table 1: Checklist for identifying ancient craters.**

606 Figure S7 shows examples of applying the checklist, and Figure S8 shows the crater maps
607 resulting from applying the checklist.

608

609

Checklist for accepting ancient craters

Must be an impact structure that is embedded within the stratigraphy.

- Crater, or crater rim (if preserved), or ejecta (if preserved) are crosscut by fluvial deposits → accept
- Crater, or crater rim (if preserved), or ejecta (if preserved) are crosscut by fluvial channels → accept
- Crater partly overlain by sediments topographically, stratigraphically or texturally continuous with surrounding layered sediments → accept
- Crater forms a rimmed circular mesa
- Crater forms a rimmed circular mesa with flat or inward-dipping strata inside the rim; these strata need not be continuous with sediment outside (and usually are not)

Other checks:

- At same or similar level and spatially adjacent to an ancient crater; has the same preservation style (e.g., layered circular mesa) as that ancient crater
- Crater is close to circular (ellipticity < 1.15)

- Rim or edge preserved topographically in DTM over at least 180° of arc (does not have to be continuous)

or

- Crater appears to be concave-up in anaglyph

if neither:

- Reject.

Ensemble checks:

- Is the same preservation style of craters found beyond the mapped background geologic unit in this geologic region? (If so, could be a younger mantling unit: reject all craters)
- Are the ellipticities aligned?
- Is the distribution of crater centers random in space?
- Do any clusters match to geology? (If so, suspect soft-sediment deformation).

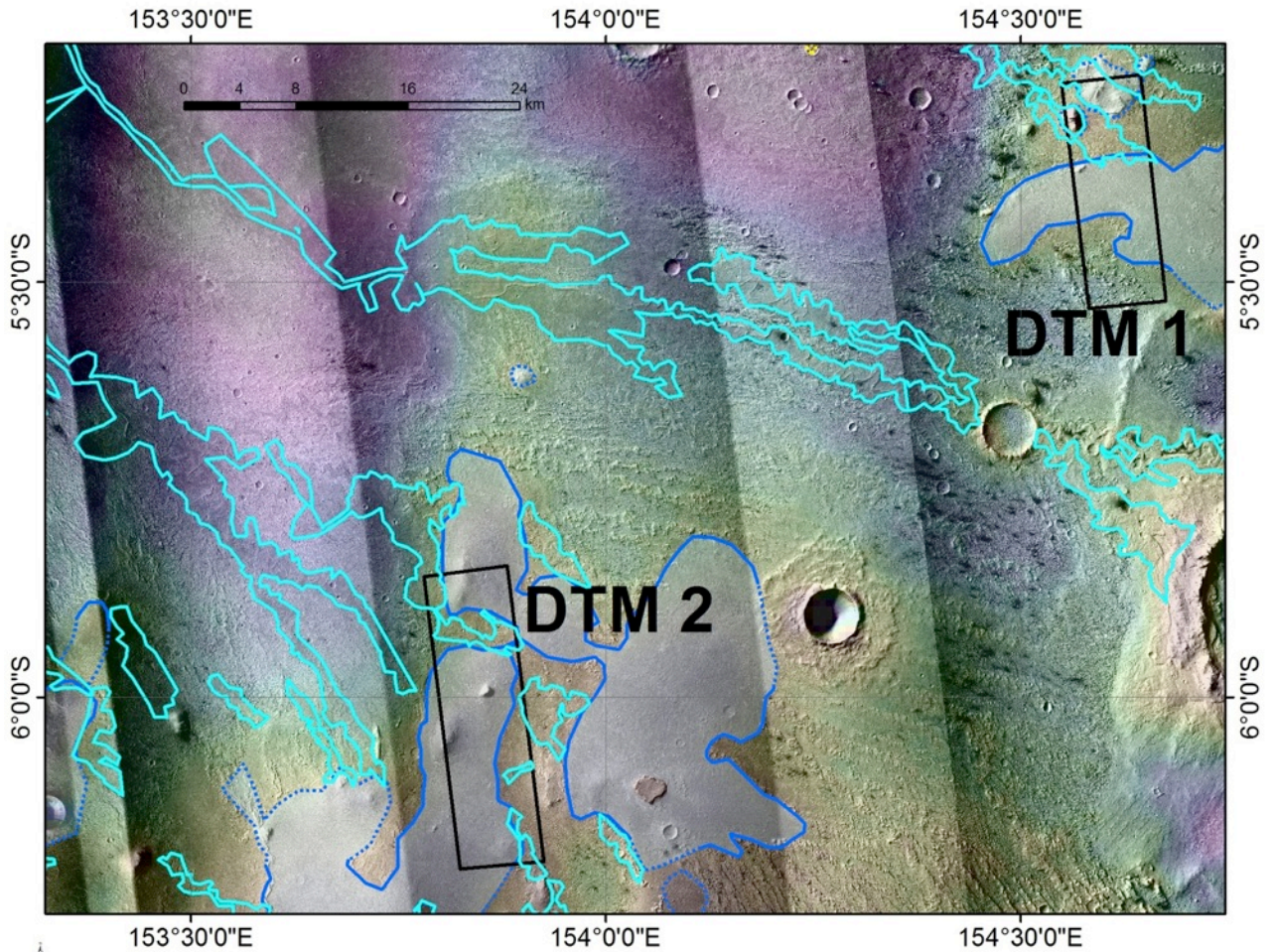
Checklist for rejecting ancient craters: rejects override accepts

Either not clearly an impact structure, or not embedded within stratigraphy

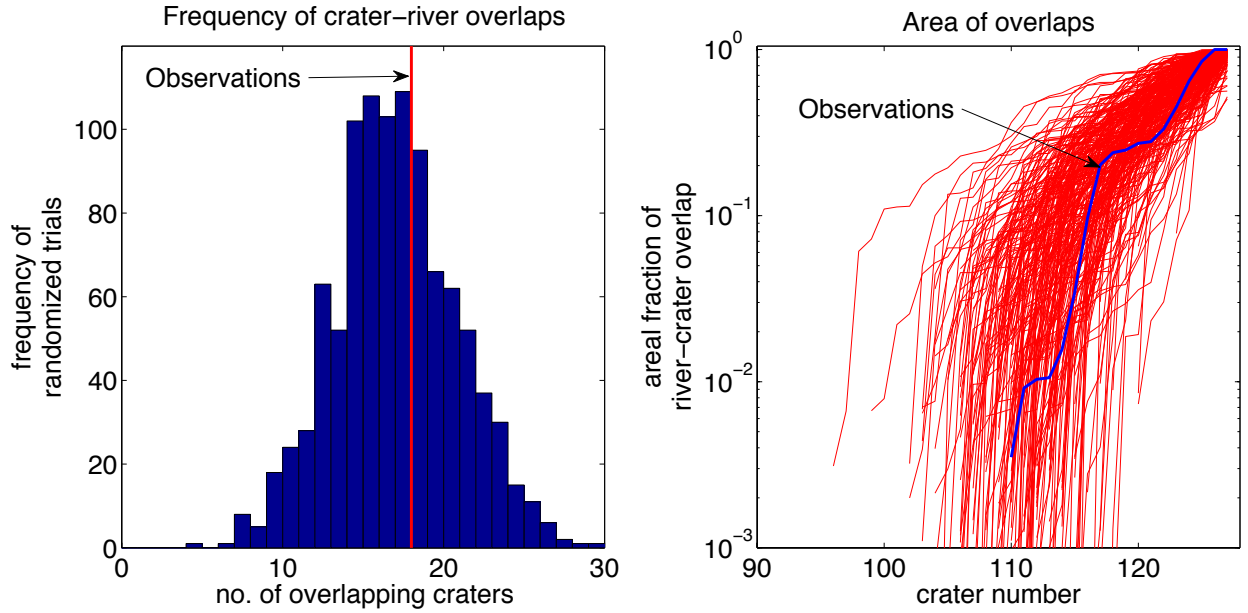
- Rim preserved mostly (>2/3) intact, and rim ellipticity > 1.5 → immediate reject
- Crater (and ejecta, if visible) are not superposed by anything other than active/recently active bedforms → immediate reject
- Rays visible → immediate reject
- Crater could be a prolongation of nearby deformation pattern with cell-shaped sediments and upcurled edges ('spatulate' soft-sediment deformation).
- (For circular mesas) The height of the mesa exceeds the radius of the flat top or rim by >1.5 (risk of being a rootless cone or explosion pit analogous to von Braun/Goddard at the Spirit field site).
- There is a rim visible around all or most of the top of the structure, but the elevation of the rim is much lower on one side of the structure (immediate reject; suggestive of volcanism or soft-sediment deformation)

Ensemble level checks for circular mesas - Is there a connection between the relief of the mesa and the diameter of the depression on top? if yes, argues for explosive cone rather than eroded/exhumed impact crater.

611 **Supplementary Figures.**

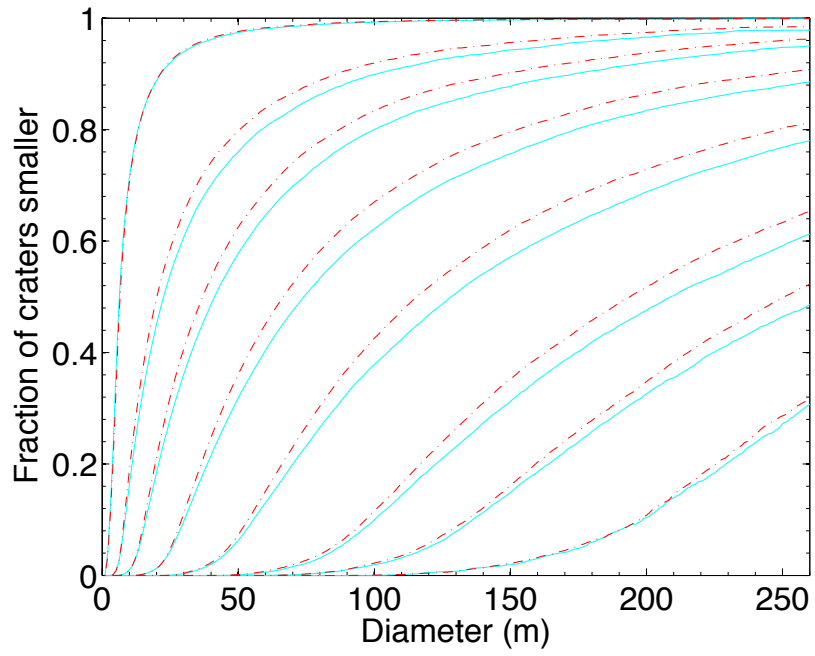


612
613 **Figure S1.** Geologic context for this study. Topographically lower fluvial unit (“F1”, no tint)
614 contains large meander belts (cyan outlines). Topographically higher fluvial unit (“F2”, white tint)
615 contains many river deposits but lacks large meander belts. F1/F2 contact is shown as a solid blue
616 line where mapped with high confidence, and as a dotted blue line where inferred. Background
617 color is cued to MOLA topography (elevation range ~ 500m). Background image is CTX mosaic.
618 DTMs were constructed from HiRISE images PSP_007474_1745/ESP_024497_1745 (DTM 1)
619 and ESP_017548_1740/ ESP_019104_1740 (DTM 2). DTM1 area is 108 km²; DTM2 area is 86
620 km². See Fig. S8 for details.



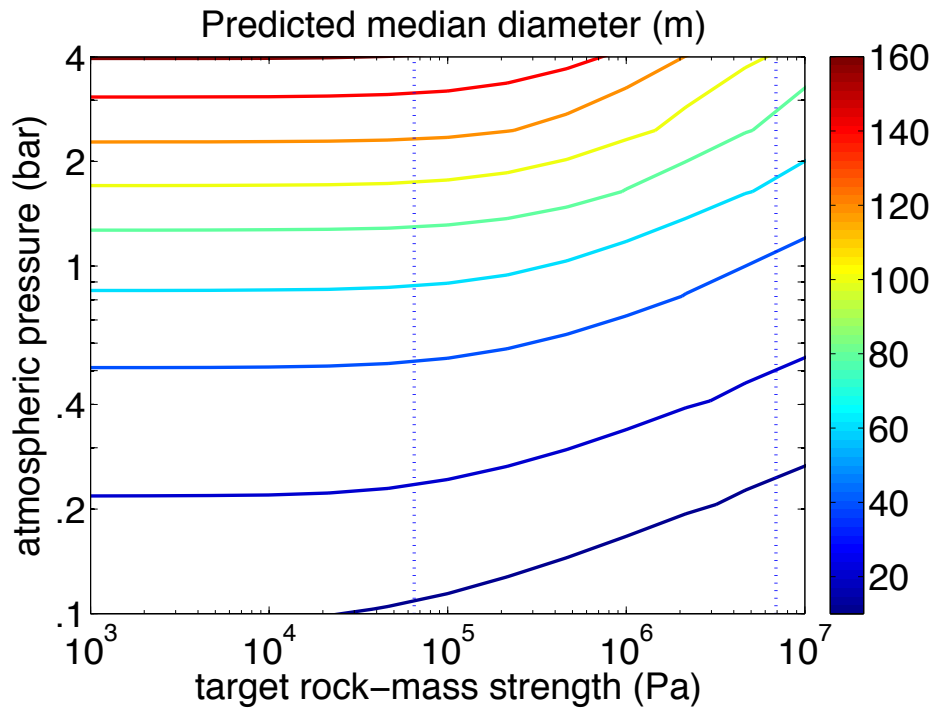
621

622 **Figure S2.** Crosscut test comparing observed crater-river interaction areas to an ensemble of 1,000
 623 synthetic crater-populations. Comparison of crater-river interactions in the observed population
 624 and an ensemble of synthetic crater populations with the same size-frequency distribution. Left
 625 panel: Frequency of crater-river overlaps for 1,000 synthetic crater populations (observations
 626 shown by vertical red line). Right panel: Fractional area of overlap for each crater – for legibility,
 627 only every fourth synthetic population is shown. Craters are sorted by fractional overlap – the
 628 majority of craters in the synthetic and observed populations have zero overlap. Observations are
 629 shown by thick blue line.



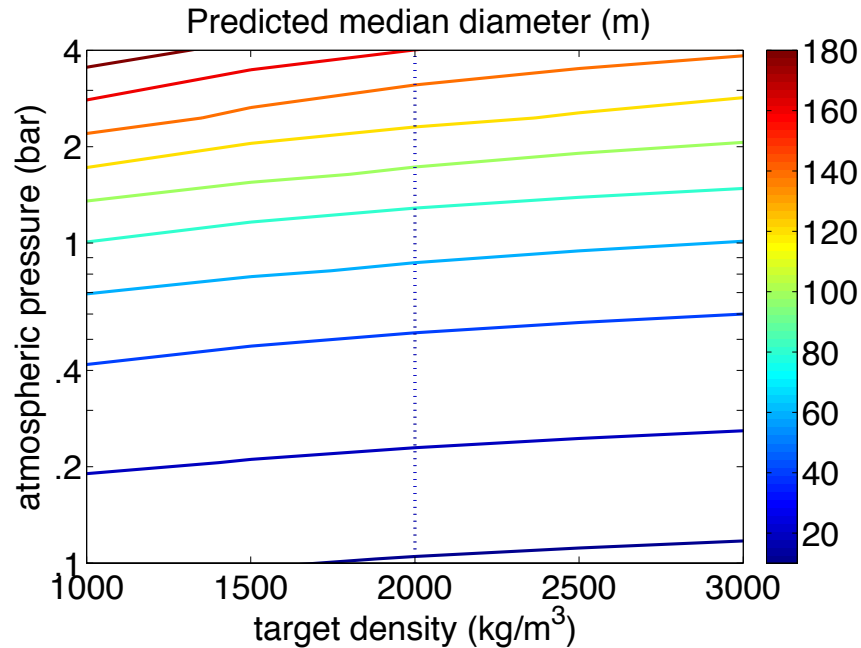
630

(a)



631

(b)

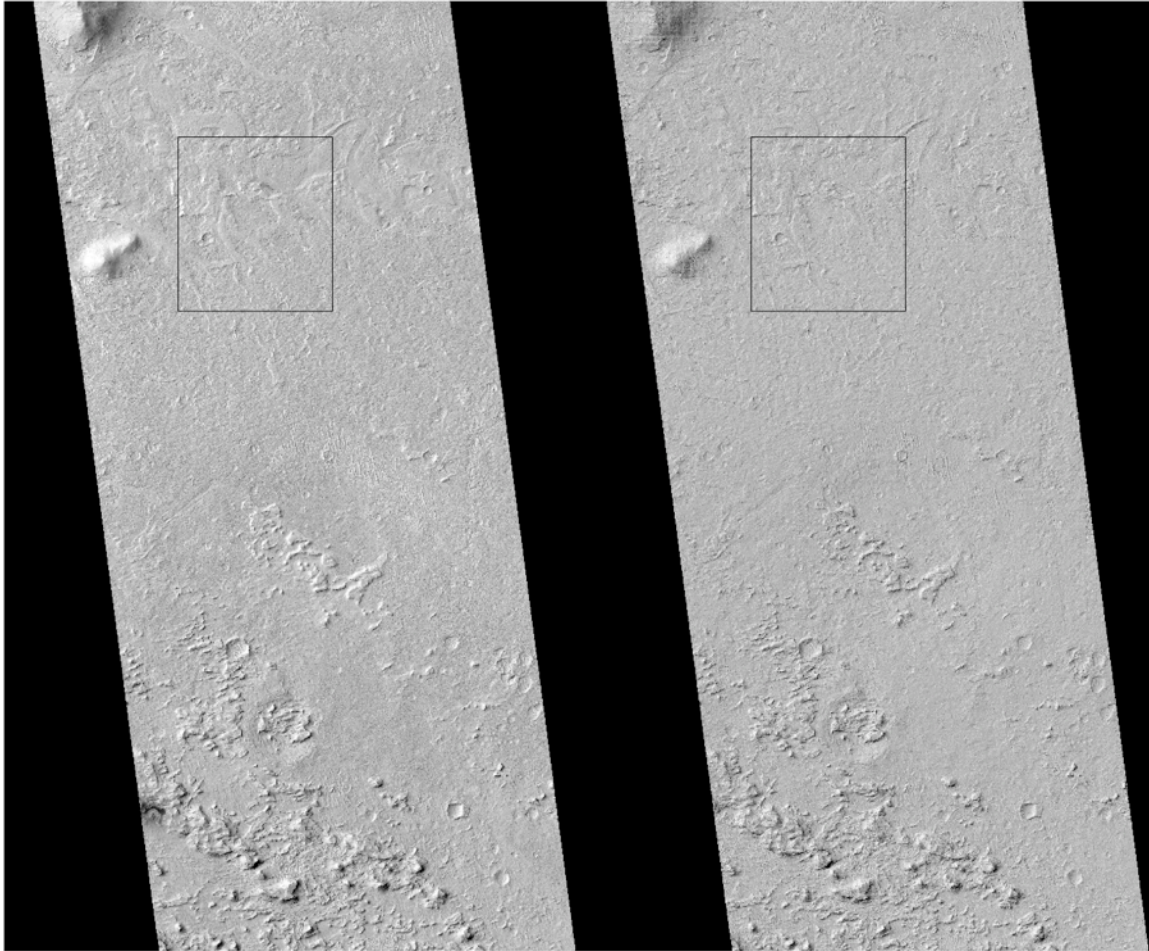


632

(c)

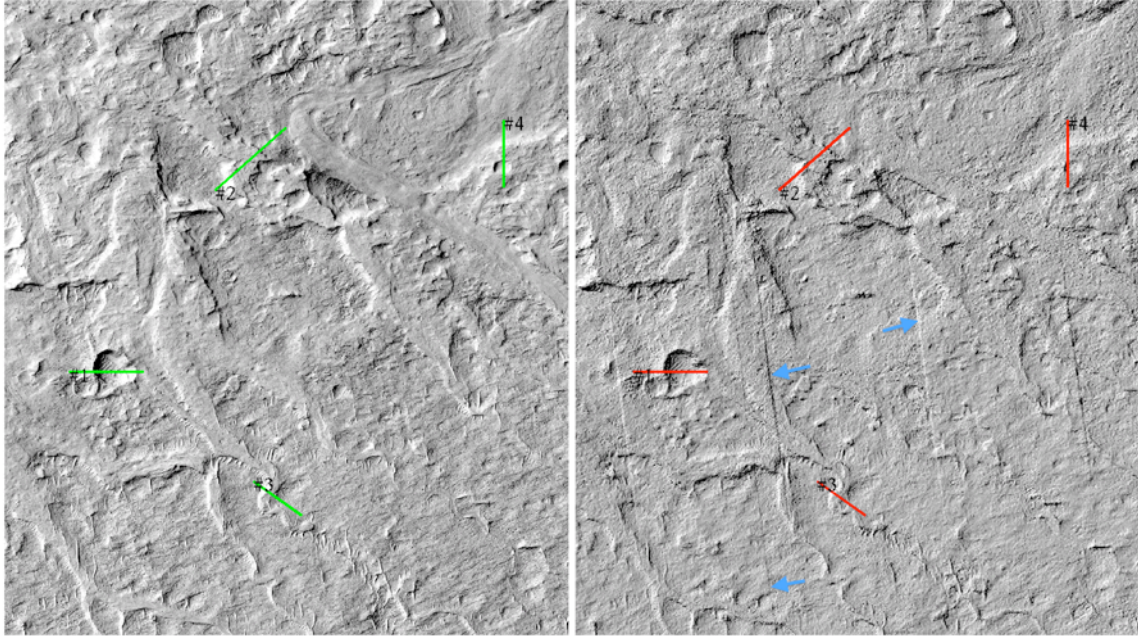
633

634 **Figure S3.** Sensitivity tests. (a) Fragmentation parameterization: cyan solid lines show crater sizes
 635 ignoring the last fragmentation event; red dashed lines show “effective” size of impact combining
 636 all fragments into one “effective” cluster. From left to right, pressures are for 6 mbar, 125 mbar,
 637 250 mbar, 500 mbar, 1 bar, 2 bar, 3 bar and 5bar (assuming impacts at 0m elevation). (b)
 638 Sensitivity to target rock-mass strength (using π -group scaling; Refs. 14, 22). Contours drawn at
 639 median crater size of 10m, 20m, 40m, and then at 20m intervals until 160m. Left vertical dashed
 640 line (65 kPa) is strength inferred for desert alluvium (Ref. 14), which is appropriate to our geologic
 641 setting. Right vertical dashed line (6.9 MPa) is “hard rocks” value used by Ref. 22 (their Figure 7).
 642 If the Aeolis Dorsa sediments had “hard rock”-like strength at the time the craters formed, then our
 643 upper limit is significantly relaxed. (c) Sensitivity to target density (using π -group scaling):
 644 Contours drawn at median crater size of 10m, 20m, 40m, and then at 20m intervals until 180m.
 645 Vertical dashed line is our preferred value (2000 kg/m³); a reasonable range is 1500 – 2500 kg/m³,
 646 for which inferred-paleopressure variations are modest.



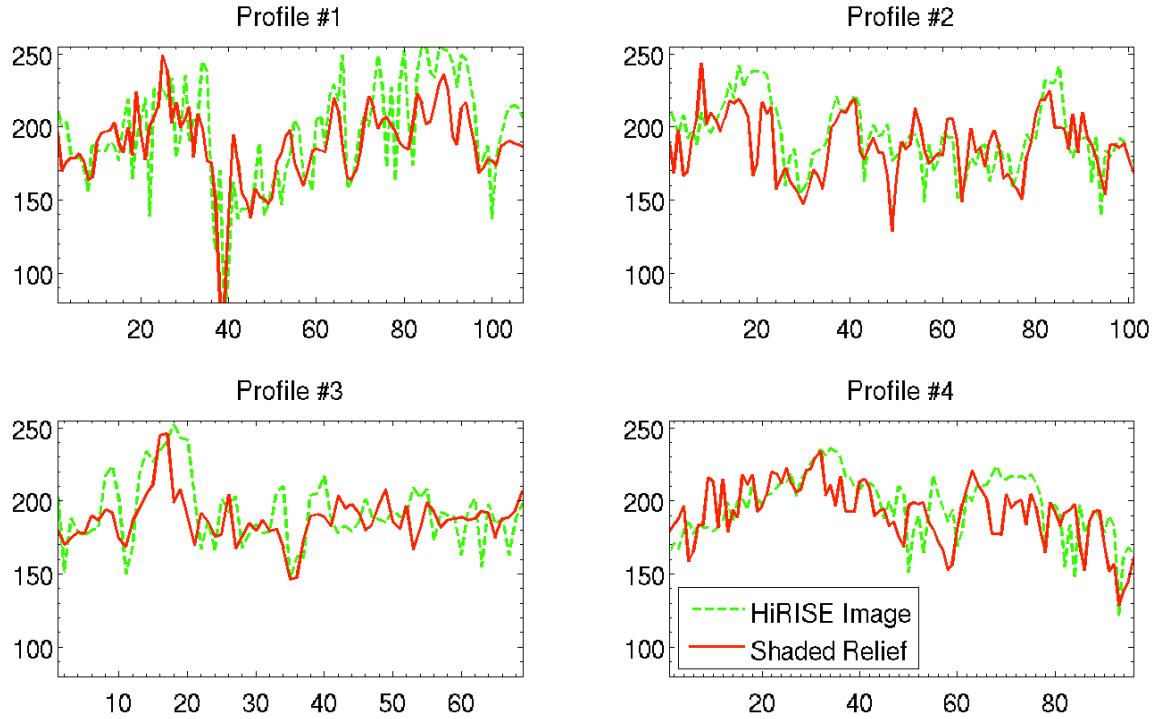
647

648 **Figure S4.** PSP_007474_1745 image on left, shaded relief of corresponding DTM (DTM1,
649 PSP_007474_1745/ESP_024497_1745) on right illuminated using the same illumination
650 geometry. Black box shows region highlighted in Fig. S5.



651

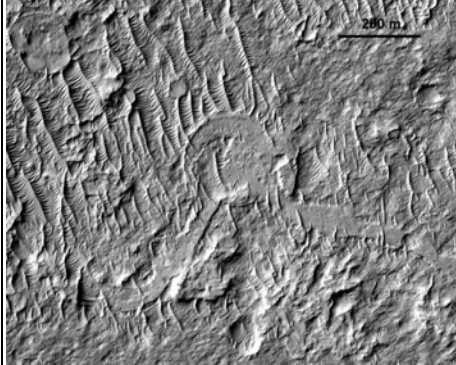
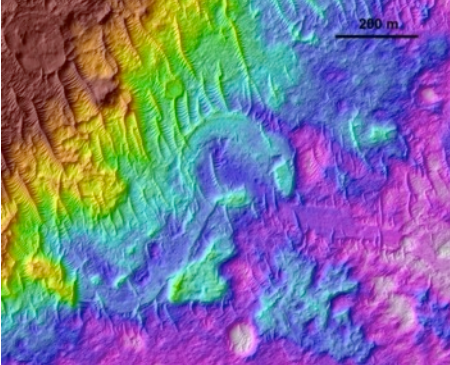
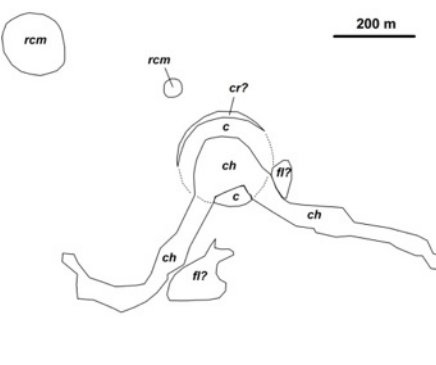
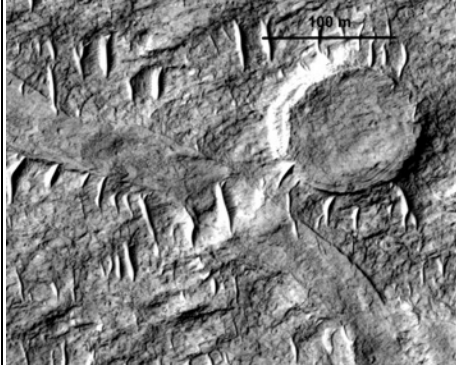
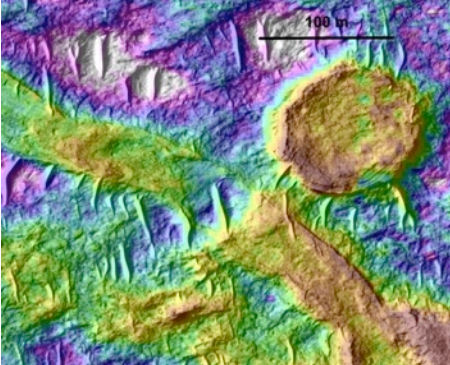
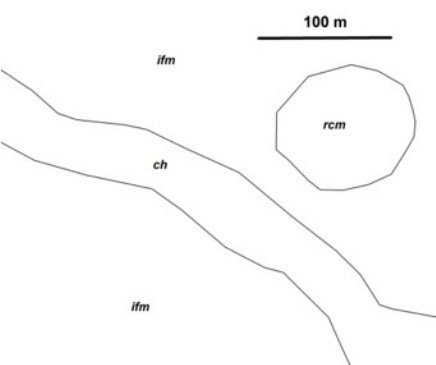

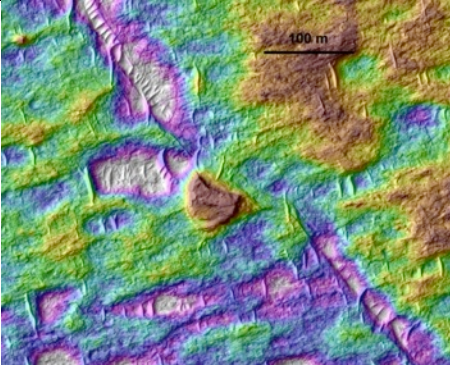
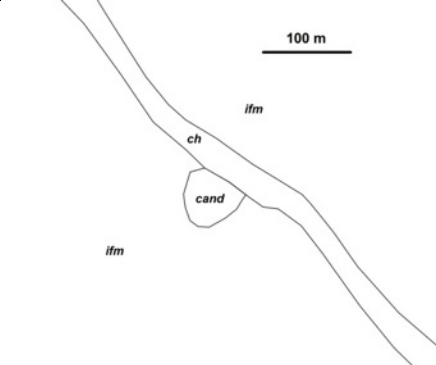
652 **Figure S5.** Comparison between HiRISE image and the stereo DTM using the same illumination
653 geometry. Left panel: PSP_007474_1745 image (25cm/pixel). Right panel: shaded relief from the
654 stereo extraction. Seams at the boundaries between HiRISE CCDs are visible in the DTM (blue
655 arrows on right panel). Their obvious presence makes it possible to take them into account in any
656 measurement. Red and green profiles correspond to the cross-sections shown on Fig. S6.



658

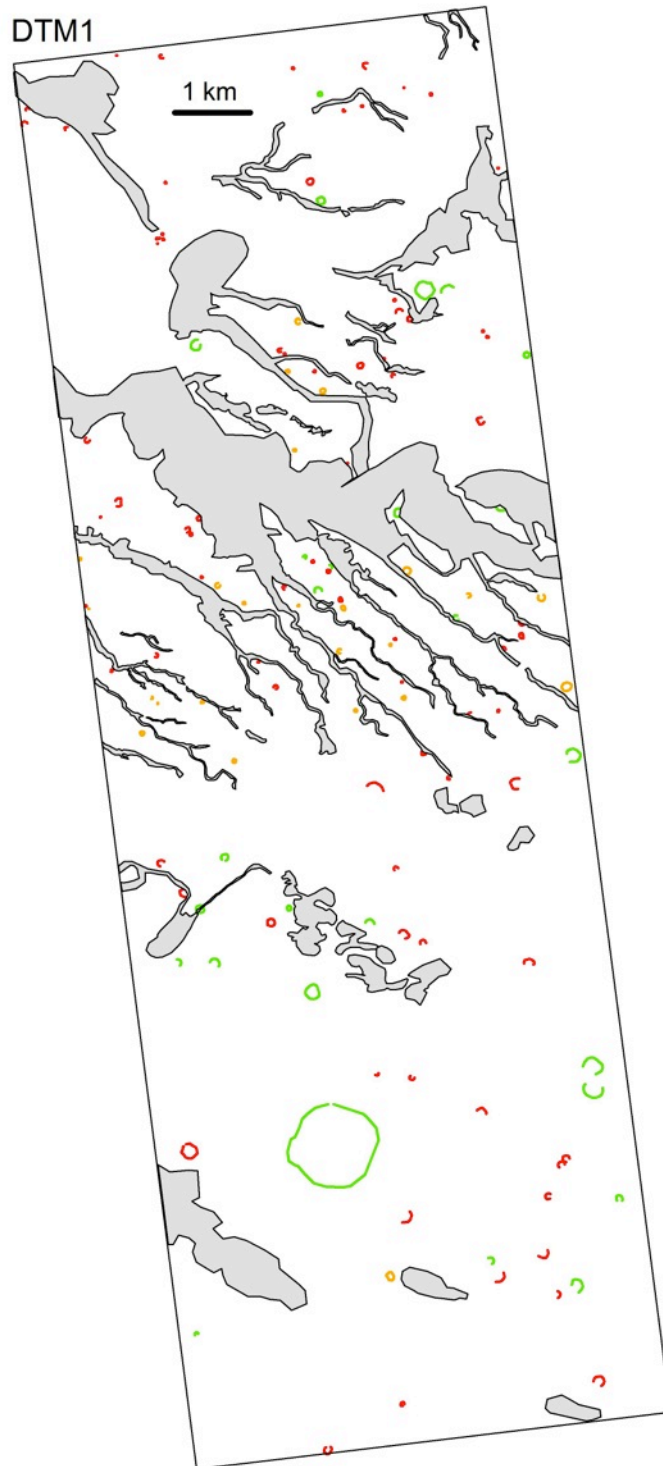
659 **Figure S6.** Cross-sections along both HiRISE image (green) and DTM shaded relief (red)
 660 computed using the actual illumination geometry. x axes correspond to distance in m, y axes
 661 correspond to nondimensional brightness. Good agreement is obtained at the DTM post resolution,
 662 highlighting the good quality of this DTM extraction.

663 **Figure S7.** Examples of application of the checklist in Supplementary Table 1 (anaglyphs not shown). DEF = definite embedded crater;
 664 RCM = rimmed circular mesa; CAND = candidate ancient crater (excluded from paleopressure calculations). Key to sketch interpretations:
 665 *c* – crater or crater fill; *cand* – candidate ancient crater; *ch* – channel or channel-fill material; *cr* – crater rim material; *fl* – fluvial deposits
 666 not part of an integrated channel; *ifm* –interfluve material (unknown origin; simplest interpretation is fluvial overbank material); *rcm* –
 667 rimmed circular mesa.

Type	Orthophoto	Orthophoto + DTM	Sketch interpretation	Notes
DEF				Crater is crosscut by fluvial deposits that are topographically and texturally continuous with those outside crater. Crater is close to circular. Rim or edge is preserved (discontinuously) over more than 180° of arc. → DEF. ESP_017548_1740. This crater is entry #8 from the Supplementary Table of Ref. 20. See also Figure 1 for additional examples of definite embedded craters.
RCM				Crater forms a rimmed mesa. Ellipticity is < 1.15. Rim is preserved (based on DTM and image shading) over more than 180° of arc. Crater appears concave-up in anaglyph and in DTM. No evidence for rays, ejecta, or nearby soft-sediment deformation of similar style. Elevation of mesa ~4m, much less than mesa diameter. → RCM. PSP_07474_1745.
CAND				Raised circular structure is truncated by channel. Subtle rim may be present, however structure is convex-up overall. Origin is unclear: one possible alternative to impact is preferential erosion around the margins of spatulate soft-sediment-deformation. → CAND. PSP_07474_1745.

668

669 **Figure S8.** Maps showing locations of:- definite ancient craters (green); rimmed circular mesas
670 (orange); candidate ancient craters (red - excluded from paleopressure calculations); channels
671 and channel belts (gray shading). In most cases crater rims are only partially preserved.



672

DTM2

